

Expanding the quantum photonic toolbox in AlGaAsOI

Cite as: APL Photonics 7, 096103 (2022); <https://doi.org/10.1063/5.0098984>

Submitted: 13 May 2022 • Accepted: 25 August 2022 • Published Online: 19 September 2022

 J. E. Castro,  T. J. Steiner,  L. Thiel, et al.



View Online



Export Citation



CrossMark

ARTICLES YOU MAY BE INTERESTED IN

[Photonic circuits for laser stabilization with integrated ultra-high Q and Brillouin laser resonators](#)

APL Photonics 7, 096104 (2022); <https://doi.org/10.1063/5.0091686>

[Reduced material loss in thin-film lithium niobate waveguides](#)

APL Photonics 7, 081301 (2022); <https://doi.org/10.1063/5.0095146>

[Perspective on the future of silicon photonics and electronics](#)

Applied Physics Letters 118, 220501 (2021); <https://doi.org/10.1063/5.0050117>



yttrium iron garnet glassy carbon beamsplitters fused quartz additive manufacturing
 zeolites III-IV semiconductors gallium lump copper nanoparticles organometallics
 nano ribbons barium fluoride europium phosphors photonics infrared dyes
 epitaxial crystal growth ultra high purity materials transparent ceramics CIGS
 cerium oxide polishing powder surface functionalized nanoparticles MRE grade materials thin film
 sapphire windows Nd:YAG silver nanoparticles perovskites beta-barium borate rare earth metals quantum dots
 osmium scintillation Ce:YAG refractory metals laser crystals
 anode lithium niobate InAs wafers dysprosium pellets MOFs AuNPs chalcogenides ZnS CdTe perovskite crystals transparent ceramics

The Next Generation of Material Science Catalogs



Expanding the quantum photonic toolbox in AlGaAsOI

Cite as: APL Photon. 7, 096103 (2022); doi: 10.1063/5.0098984

Submitted: 13 May 2022 • Accepted: 25 August 2022 •

Published Online: 19 September 2022



View Online



Export Citation



CrossMark

J. E. Castro,¹ T. J. Steiner,² L. Thiel,¹ A. Dinkelacker,¹ C. McDonald,¹ P. Pintus,¹ L. Chang,¹ J. E. Bowers,^{1,2} and G. Moody^{1,a)}

AFFILIATIONS

¹Electrical and Computer Engineering Department, University of California, Santa Barbara, California 93106, USA

²Materials Department, University of California, Santa Barbara, California 93106, USA

^{a)}Author to whom correspondence should be addressed: moody@ucsb.edu

ABSTRACT

Aluminum gallium arsenide-on-insulator (AlGaAsOI) exhibits large $\chi^{(2)}$ and $\chi^{(3)}$ optical nonlinearities, a wide tunable bandgap, low waveguide propagation loss, and a large thermo-optic coefficient, making it an exciting platform for integrated quantum photonics. With ultrabright sources of quantum light established in AlGaAsOI, the next step is to develop the critical building blocks for chip-scale quantum photonic circuits. Here we expand the quantum photonic toolbox for AlGaAsOI by demonstrating edge couplers, 3 dB splitters, tunable interferometers, and waveguide crossings with performance comparable to or exceeding silicon and silicon-nitride quantum photonic platforms. As a demonstration, we de-multiplex photonic qubits through an unbalanced interferometer, paving the route toward ultra-efficient and high-rate chip-scale demonstrations of photonic quantum computation and information applications.

© 2022 Author(s). All article content, except where otherwise noted, is licensed under a Creative Commons Attribution (CC BY) license (<http://creativecommons.org/licenses/by/4.0/>). <https://doi.org/10.1063/5.0098984>

I. INTRODUCTION

Photonic integrated circuits (PICs) have already shown promise as platforms for quantum information.^{1–6} However, development of PICs for problems of interest in fields such as communication, computing, sensing, and metrology will require circuits with both scale and functional complexity well beyond even the most mature of quantum PICs (QPICs). QPIC functionality of any complexity relies on a small set of components for on-chip manipulation of quantum states of light, including active modulators and switches as well as passive routing components, beam splitters, and on/off chip couplers.⁷ The largest demonstrations to date using these components and on-chip photon sources have been realized on silicon,^{2,8} whose swift progress as a quantum photonic platform has benefited from its prominence in classical photonics and the complementary metal oxide semiconductor (CMOS) industry. Other demonstrations include material platforms such as silicon nitride,^{5,9} aluminum nitride,¹⁰ lithium niobate,^{11,12} and indium phosphide,¹³ however, no single platform clearly wins out on performance across all metrics, including material absorption, waveguide propagation

loss, $\chi^{(2)}$ and $\chi^{(3)}$ nonlinearities, and thermo-optic coefficients for tuning and modulation. Recent improvements in fabrication have opened the possibility of alternative materials with better suitability toward specific functionalities than silicon, such as the aluminum gallium arsenide-on-insulator (AlGaAsOI) platform.¹⁴

As a QPIC platform, AlGaAsOI is attractive for its large $\chi^{(2)}$ and $\chi^{(3)}$ nonlinear coefficients, which enable more efficient spontaneous parametric down conversion (SPDC) and spontaneous four wave mixing (SFWM) than silicon, strong modal confinement due to its large refractive index,¹⁵ a thermo-optic coefficient comparable to silicon for efficient tuning,^{16–18} and electro-optic¹⁹ and piezo-optic²⁰ effects for cryogenic tuning. Additionally, varying the aluminum content of AlGaAs enables bandgap engineering such that two-photon absorption, a major challenge in silicon QPICs, is minimal at telecommunication wavelengths.²¹ Until quite recently, the utility of the AlGaAsOI platform has been restricted by high waveguide propagation loss.²² Improvements in the fabrication process¹⁴ have reduced propagation losses to less than 0.2 dB/cm, enabling demonstrations of microring resonators with quality factors above 3×10^6 . In combination with low material absorption and a large $\chi^{(3)}$

nonlinear coefficient, this has led to record-low Kerr comb generation threshold powers and entangled photon pair sources 1000 times brighter than state-of-the-art in silicon.^{23,24} For applications in optical computing, the Knill Laflamme Milburn (KLM) protocol²⁵ can be realized with scalable architectures that only require linear optical interferometers and waveguide crossers (reported here), single photon sources (shown in our previous manuscript²⁴), and single-photon detectors (available commercially and also on-chip²⁶). While the manufacturability of AlGaAsOI is currently at the level of small-scale, chip-sized QPICs, previous demonstrations of wafer-scale bonding^{27,28} lay out a path toward scalable AlGaAsOI photonics and its application to quantum information technologies. Yet, because of its novelty, the AlGaAs platform has lacked the same level of individual circuit component development as more established platforms including silicon and silicon nitride.

Here, we report on high-performance AlGaAsOI components, including edge couplers, waveguide crossings, and tunable interferometers that, along with previously demonstrated ring resonator sources, form the foundation of a functional on-chip platform with potential not only in QPICs but classical PICs as well, including applications in optical communications and spectroscopy.^{29–31} Low-loss chip-to-fiber couplers are necessary both in the near term for interfacing with off-chip light sources and detectors, and further in the future for networking of smaller resource-state chips as parts of larger architectures. Waveguide crossers enable more complex circuit design where interactions between non-next nearest-neighbor qubits are necessary. Since the circuit elements are all fabricated using the same photonic layer, the routing requires waveguide crossers with minimal loss and crosstalk to adjacent channels. Interferometers serve many purposes for on-chip optical programming schemes, including pump filtering, de-multiplexing distinct frequency modes, acting as beam splitters, and serving as linear optical quantum gates. The development of these components opens the door for demonstrations of chip-scale QPICs using the AlGaAsOI platform, leveraging the benefits that AlGaAs offers over silicon and other nonlinear optical platforms.²⁸ The components described below are designed assuming eventual full integration with AlGaAsOI ring resonator entangled-photon pair sources optimized for $\chi^{(3)}$ spontaneous four-wave mixing such as that detailed in Ref. 24. As an example, Fig. 1 shows a quantum photonic circuit for chip-scale Boson sampling to illustrate the opportunities that the

development of interferometers and waveguide crossers can enable. The individual components are highlighted where they may reside in complex quantum photonic circuitry. In the remainder of this manuscript, we describe the design, simulation, and experimental results of many of the fundamental components of a quantum photonic platform.

II. QUANTUM PHOTONIC TOOLBOX

All of the components were fabricated using an AlGaAs photonic layer grown via molecular-beam epitaxy (MBE). The full fabrication procedure has been detailed previously.^{23,24} Briefly, a GaAs chip with a 400-nm-thick AlGaAs photonic layer is bonded onto a 3- μm -thick thermal SiO₂ buffer layer on a Si substrate. After removing the substrate through selective wet etching, the AlGaAs surface is passivated using an 8 nm film of Al₂O₃ grown via atomic layer deposition (ALD). Deep ultraviolet photolithography is used to pattern photoresist, which is used to etch a SiO₂ hardmask and then the AlGaAs photonic layer to define the components. Another ALD deposition of Al₂O₃ passivates the surface before a 1.0 μm thick SiO₂ cladding layer is deposited. Finally, 10 nm of titanium and 100 nm of platinum are deposited as resistive heaters for thermo-optic tuning.

A. Edge couplers

Before a fully integrated QPIC is fabricated, it is necessary to utilize either fiber-based or free-space optical testing instruments. Thus, one of the first components to design is an efficient structure to couple light into and out of the photonic chip. Various strategies have been explored for efficient coupling,³² but many of the methods that achieve ultra-high efficiency require additional fabrication steps—electron-beam lithography, anti-reflection coatings, or a full redesign of the input/output facet structure. For high throughput testing of individual components, much simpler structures can be used; as long as the fiber-to-chip coupling efficiency can be adequately characterized, any undesirable effects due to the input/output coupling can be isolated from the component performance.

There are two main categories of fiber-to-chip couplers: vertical couplers and edge couplers (also called “in-plane” and “butt” couplers, respectively). As the name suggests, vertical couplers accept incoming light from the top of the chip (out of plane), while

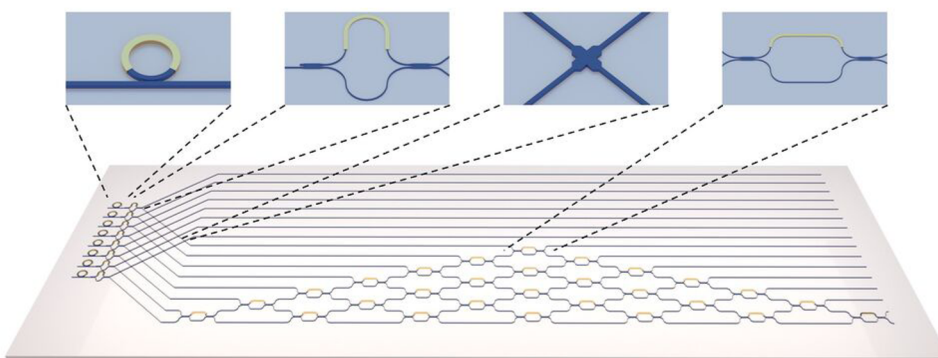


FIG. 1. Illustrative example of a programmable QPIC for on-chip optical computing and communications, shown here as a generic m -mode unitary operator for Boson sampling. A general platform comprises: (i) tunable microring resonators or waveguides for quantum light generation; (ii) tunable unbalanced Mach-Zehnder interferometers for filters and qubit de-multiplexers; (iii) waveguide crossings for connecting non-nearest neighboring qubits; and (iv) tunable balanced Mach-Zehnder interferometers for linear optical programming.

edge couplers couple light impinging from one of the facets of the photonic chip (in plane). Depending on the desired application or testing design, there may be a benefit for utilizing either type of coupler. Vertical couplers are useful for more compact designs as they do not require waveguides to be routed completely to the edge of the photonic chip.³³ Generally, vertical couplers utilize periodic gratings that satisfy the Bragg condition in the waveguide to couple light into an optical fiber oriented almost perpendicular to the surface.^{33,34} Edge couplers, on the other hand, can be much simpler to design and less sensitive to fabrication variation. Instead of relying on grating-based structures, edge couplers manipulate the waveguide dimensions to expand the waveguide mode to be closer matched with the mode in the fiber.³⁵ The easiest way to achieve this conversion is to taper the waveguide to a narrow tip (called an “inverse taper”) where the mode becomes weakly confined and expands closer to the mode size of the fiber. A standard taper, where the waveguide width is expanded at the facets, can also serve as an edge coupler. However, in high-index contrast platforms, the design typically has lower efficiencies since the strongly confined mode will remain smaller than the fiber mode. The waveguide becomes capable of supporting multiple modes, and the high-index contrast produces large backreflections.³⁵ Other edge coupling strategies include utilizing multiple inverse tapers in a trident or dual-tip design,³⁶ polymer-based spot size converters,³⁷ or multi-layer spot size converters.³⁸ Due to the much simpler design, here we report only on inverse taper AlGaAsOI edge couplers. A scanning electron microscope (SEM) image of several inverse tapers is shown in Fig. 2(a). The facet is on the right side of the image, and the waveguides taper from 600 nm width (on the left) down to 200 nm at the facet. For a more in-depth study of the various types of coupling strategies, readers are referred to Ref. 32, which highlights various vertical and edge coupling strategies on the silicon-on-insulator (SOI) platform.

The inverse taper design reduces the confinement of the waveguide mode, increasing its effective modal area and decreasing its effective index of refraction. This allows for moderately high simulated coupling efficiencies (losses <3 dB) to a (typically) lensed fiber aligned with the waveguide facet. The overall coupling loss is determined by effects such as reflection at the chip facet (due to refractive index mismatch), fiber-to-waveguide mode mismatch, and mode-conversion within the waveguide taper.

To determine the optimal design for an inverse taper edge coupler, the dimensions of the waveguide taper were varied and simulated using Lumerical MODE software. Here, we show only the results for inverse tapers designed for the fundamental transverse electric (TE) mode because the components shown in the rest of this article are designed to operate with TE polarized light. Similar calculations can be made for the transverse magnetic (TM) mode. For a given Gaussian beam and waveguide geometry, the power overlap between the waveguide mode and fiber mode is calculated to estimate an upper bound on coupling efficiency and determine the optimum waveguide dimensions. This calculation does not include loss due to mode conversion or reflection at the interface. Figure 2(b) illustrates the simulated mode overlap between a Gaussian beam with a mode field diameter of 2.5 μm (which matches the mode field diameter of commercially available lensed fibers) and a 400 nm thick AlGaAsOI waveguide with various taper widths. Narrow taper widths enlarge the waveguide mode to be nearly mode-matched with the incoming fiber mode, but the weak confinement of these narrow waveguides typically comes with additional loss as light propagates through the narrow taper back to a waveguide width of ≥ 400 nm for the components. The fabrication of sub-200-nm features is challenging using the standard photolithography process; so, we limit our taper designs to 200 nm or larger. Along with the simulated data, Fig. 2(b) also shows a measured value for the coupling loss for a 200 nm edge coupler at a wavelength of 1550 nm. The measured value was collected by sending 6.95 dBm (~ 5 mW) of light into a straight waveguide with 200 nm tapers on the input and output facet. The collected power through the waveguide was 1.16 ± 0.23 dBm, indicating an approximate loss of 2.9 dB/facet (the waveguide propagation loss is <1 dB/cm and the waveguide is less than 2 mm; so, the contributions of propagation loss are ignored in this measurement). The measured loss is larger than the simulated mode overlap, which is expected because the measurements also include reflections and mode conversion loss in the taper. The simulated mode overlap acts as an upper bound for the efficiency of the inverse taper. The 2.9 dB/facet of coupling loss in the AlGaAsOI platform is similar to the sub-3 dB coupling loss expected from standard SOI inverse taper edge coupler designs.³⁵ The use of narrower taper widths [as shown in Fig. 2(b)] or an anti-reflection coating will improve the coupling efficiency further, but ease of fabrication and reliability are prioritized; so, for our initial devices, 200 nm inverse tapers are utilized.

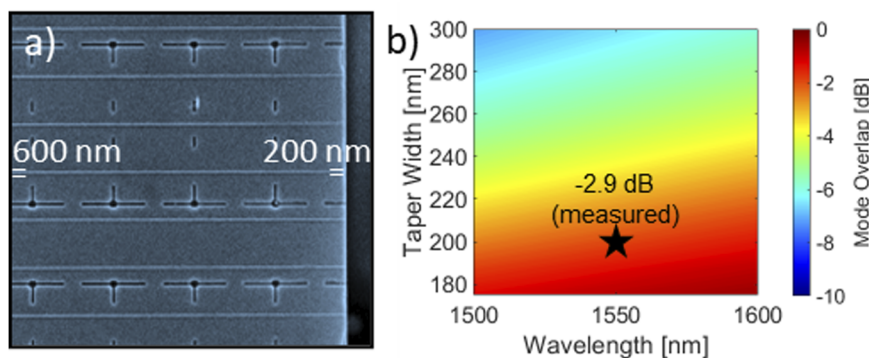


FIG. 2. (a) Scanning electron microscope (SEM) image of an array of inverse taper edge couplers. (b) Simulated mode overlap between a 2.5 μm Gaussian beam and an AlGaAsOI waveguide for various widths of the input taper and a fixed height of 400 nm. The star indicates an experimental measurement of the coupling loss through a straight waveguide device with 200 nm input/output couplers.

B. Waveguide crossings

Several methods have been explored for creating low-loss waveguide crossings including vertical coupling into polymer strip waveguides,³⁹ multi-planar crossings,⁴⁰ multimode interference-based crossings,^{41–43} and subwavelength gratings.⁴⁴ Many of these methods involve additional fabrication steps that can introduce excess loss and system design and fabrication challenges. A basic approach for waveguide crossing relies on tapering an input single-mode waveguide section into a larger waveguide cross section that can support higher-order modes and relies on the beating between the fundamental mode and the higher-order mode to create an electric field maximum that is centered in the waveguide at the crossing location. By focusing the mode into the center of the wide waveguide, evanescent coupling to the perpendicular waveguide is minimized. This design can be completed with a basic linear taper (which will be referred to as a “simple crossing”) or a more complex structure. Here, we consider simulations of both simple and inverse-design crossings and report results from an inverse design approach (which will be referred to as a “13-width crossing”) that utilizes 13 different widths in a parabolic taper that requires no additional fabrication steps and maintains low-loss, high-isolation transmission. The second design utilizes a swarm optimization protocol such that the optical mode is transmitted with minimal coupling to the crossed waveguide.

The simple crossing design is illustrated in Fig. 3(a) and uses the beating between the fundamental and higher-order mode to create a confined optical mode centered at the location of the crossing. The beat length, L_π , is defined as $L_\pi = \pi/(\beta_0 - \beta_1)$, where $\beta_{(0,1)}$ is the propagation constant of the fundamental waveguide mode and first-order waveguide mode, respectively. For a $1.5 \mu\text{m}$

multimode waveguide width (w_m), the fundamental and first-order TE modes have effective indices of ~ 3.00 and 2.87 , respectively, at a wavelength of 1550 nm . Using these effective indices, the beat length is calculated as $5.95 \mu\text{m}$. Finite difference time domain (FDTD) simulations were utilized to account for the transition region between the single-mode waveguide and the wider, multimode waveguide as well as allow for a larger bandwidth crossing to be designed where the average loss across a 100 nm bandwidth is utilized instead of maximizing at a single wavelength. The simulated mode profile for the simple crossing design and the simulated transmission through the device is shown in Figs. 3(b) and 3(c), respectively. From the mode profile simulation, it is clear that the beating between the fundamental and higher order mode creates a local maximum at the location of the crossing that minimizes the optical mode scattered into the perpendicularly oriented waveguide. The simulated loss through this structure is 0.15 dB at a wavelength of 1550 nm .

Figure 3(d) shows the 13-width waveguide crossing with critical dimensions depicted. This design utilizes a swarm optimization protocol in an FDTD solver to optimize the transmission through the crossing by allowing the width to vary at 13 equally spaced sections along the taper. A parabolic interpolation between the 13 widths ensures a smooth transition between the various widths. The 13-width crossing design was also optimized for a bandwidth of 100 nm to maintain a low-loss performance of the crossing across a broad bandwidth, which will be compatible with broadband entangled photon pair generation in quantum photonic circuits. Lower loss structures can be made when optimizing for a smaller bandwidth. Starting with an input waveguide width of 400 nm and total crossing length (L) of $9 \mu\text{m}$, the optimizer was allowed to vary the widths w_2 – w_{13} between 200 and 2000 nm .

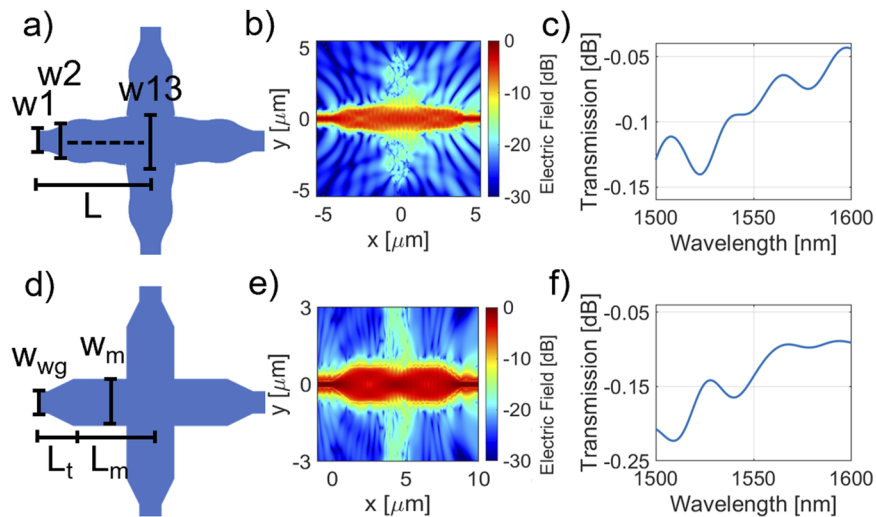


FIG. 3. (a) Schematic of the simple waveguide crossing design. The relevant design variables are indicated on the image. (b) Simulated mode profile for the optimized simple crossing design. The beating between the higher order modes and the fundamental mode results in a maximum electric field intensity in the center of the waveguide at the crossing, which minimizes the coupling to the vertical waveguide. (c) Simulated transmission through the simple waveguide crossing as a function of the wavelength. (d) Schematic of the 13-width crossing design where a swarm optimization varies the width of the parabolic taper at 13 locations and minimizes the transmission loss. (e) Simulated mode profile of the optimized 13-width crossing. (f) Simulated transmission through the 13-width crossing design as a function of wavelength.

Figure 3(e) shows the electric field profile for the optimal crossing design at a wavelength of 1550 nm, and Fig. 3(f) plots the simulated transmission through the waveguide crossing as a function of the input wavelength. This crossing design has a simulated loss of ~ 0.1 dB at a wavelength of 1550 nm. Since the loss of the 13-width crossing design is smaller than the simple crossing design, the 13-width crossing was fabricated and tested initially.

With the simulated waveguide crossing loss of the order of 0.1 dB, the cutback method⁴² is used to measure the loss per crossing to remove the coupling-dependent loss and reduce detector sensitivity limitations. For the 13-width crossing, waveguides between 10 and 50 crossings were fabricated, and the loss through each line of crossing was measured across eight trials with complete re-alignment of the input and output fibers for each trial to remove any systematic variations due to coupling loss. Figure 4(a) shows a microscope image of few of the waveguide crossings in one of the lines. The vertical waveguide channels are terminated with tapered waveguides in spiral geometry to prevent backreflections into the crossing. The horizontal spacing of the crossings is varied randomly between 25 and 35 μm to avoid photonic cavity effects. Using the cutback method, the transmission through the crossings was measured at a wavelength of 1550 nm, and the results are shown in Fig. 4(b). The dashed line indicates a linear fit of the loss as a function of the number of crossings, providing an estimated loss of 0.23 dB/crossing. The error bars on the data points indicate the standard deviation of the eight independent measurement trials.

These results for the 13-width waveguide crossing [Fig. 3(b)] indicate that the fabricated crossings have slightly higher loss than the simulated loss at a wavelength of 1550 nm. This additional loss is likely due to fabrication variations in the widths along the device; the inverse design is more sensitive to fabrication variation than the use of a simple waveguide crossing. The measured 0.23 dB of loss for the AlGaAsOI 13-width crossing is comparable to the 0.2 dB of insertion loss reported from a genetic algorithm-designed SOI waveguide crossing⁴⁵ and less than the loss of 0.3 dB from silicon nitride waveguide crossings.⁴⁶ Other manuscripts report ≤ 0.1 dB of insertion loss for elliptical tapers⁴⁷ and even of the order of 0.02 dB for sub-wavelength grating-based structures.⁴⁸ Reference 43 compares various results of waveguide crossing on the SOI platform.

C. 3 dB couplers multimode interferometers and directional couplers

A standard building block in both classical and quantum PICs is the 3 dB coupler. In QPICs, 3 dB couplers are utilized as their classical counterparts to distribute light evenly between two waveguides, to interfere single photons, and to serve as a component for tunable Mach–Zehnder interferometers (MZIs) for programmable PICs. This places strict requirements on the devices, such as low loss for potential scalability, a large bandwidth to support broadband quantum light generation, and precise splitting ratios to maximize the extinction ratio (ER) and minimize cross-talk in MZIs. We explore two designs for creating on-chip 3 dB couplers: multimode interferometers (MMIs) and directional couplers (DCs). MMIs are based on the self-imaging principle, similar to the aforementioned simple waveguide crossings; however, unlike in the waveguide crossing design, the beat length between the two modes, L_π , is used to calculate the core length necessary to achieve a splitting ratio as close to 3 dB as possible. The second coupler design based on DCs uses the overlap of evanescent modes between two neighboring waveguides, allowing the mode to fully couple into the adjacent waveguide. The full crossover length relies on the difference in refractive index between the even and odd supermodes created when two waveguides are in close proximity. DCs are straightforward couplers to design and are capable of any splitting ratio by adjusting the coupling length, but they are also more susceptible to fabrication imprecision and errors compared to MMIs.

Figure 5 depicts two MMI and DC designs and results from FDTD simulations. For the MMIs, a core width of 2.1 μm was selected. Because the self-imaging length scales with the MMI core width, a narrow width was chosen to reduce the component footprint. Symmetric input and output tapers expand the mode from a waveguide width of 0.4 μm to 0.9 μm nearest to the core. A 0.3 μm separation leaves no excess core width beyond the dimensions of the tapers in an effort to reduce Fabry–Pérot effects due to reflections. The core length design began by first calculating the beat length and multiplying it by a factor of 1.5, resulting in $L_\pi = 18.75 \mu\text{m}$. The full device was then simulated using FDTD, and the electric field profile is shown in Fig. 5(b). With a combination of the calculated beat length and FDTD simulations, a core length of 17.2 μm was chosen. The 1.55 μm difference between both methods is due to the input taper expanding the mode prior to reaching the MMI core not being considered during the beat-length calculation.

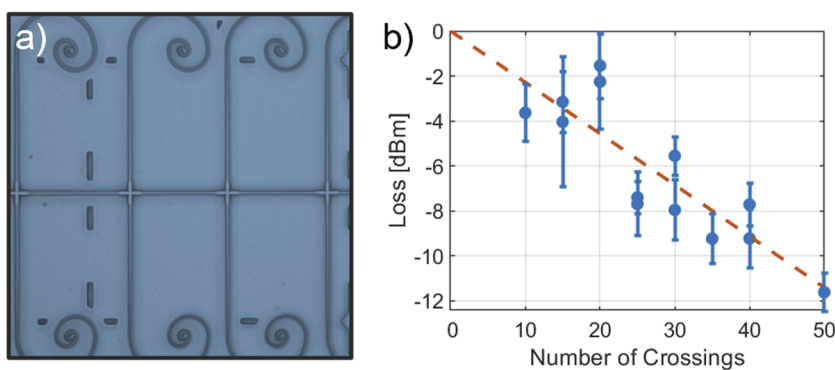


FIG. 4. (a) Optical image of cascaded waveguide crossings for loss characterization. (b) Normalized waveguide crossing transmission loss at a wavelength of 1550 nm using the cutback method. The orange trend line indicates an insertion loss of 0.23 dB/crossing.

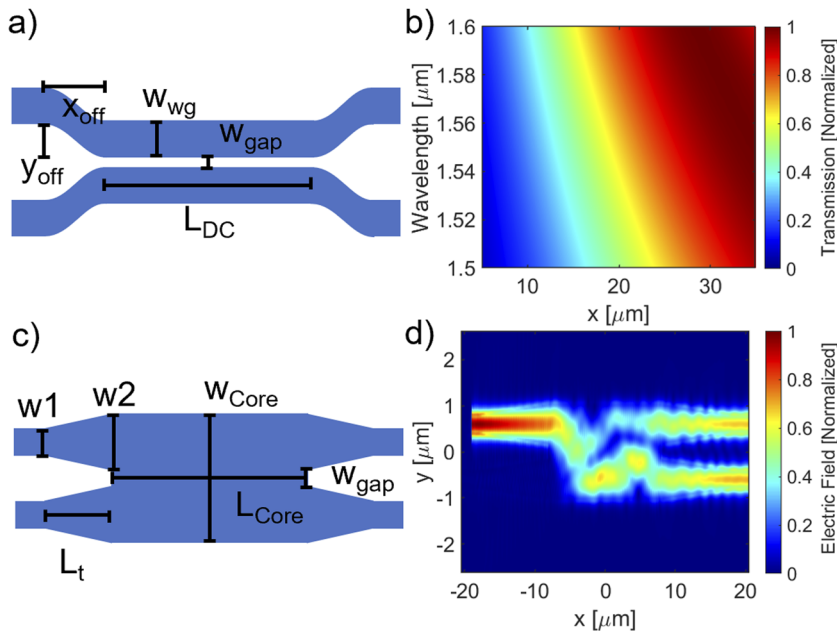


FIG. 5. (a) Schematic of a directional coupler with the relevant design parameters. (b) Simulated transmission of various directional coupling lengths to determine the appropriate coupling length for a 3 dB directional coupler. (c) Schematic of a multimode interferometer with the relevant design parameters. (d) Simulated mode profile of an MMI depicting 3 dB coupling behavior with a length near $16.0 \mu\text{m}$.

Unlike the MMIs, the DC design utilizes the same waveguide width, $0.4 \mu\text{m}$, across the entire device. Symmetric sine bend waveguides on the input and outputs with transverse displacements of 1.0 and $8.0 \mu\text{m}$ enable light to propagate near the coupling region. The minimum radius of these sine bends is kept to $20 \mu\text{m}$ to reduce bending loss. The separation between the waveguides in the coupling region where the evanescent modal overlap occurs is $0.3 \mu\text{m}$. The coupling length for the full transfer of light from one waveguide to the other was first calculated with $L = \frac{\lambda}{2(n_{(0,1)} - n_1)}$ to give an estimate of the full crossover length of the mode, where $n_{(0,1)}$ is the effective index of the even supermode and odd supermode, respectively, that exists when the two waveguides are brought in close proximity. The finite difference eigenmode (FDE) result for the full crossover length is $48.47 \mu\text{m}$. Thus, for a 3 dB coupler, $L = 24.23 \mu\text{m}$. A sweep of the coupling region using FDTD simulations of the full DC structure is depicted in Fig. 5(d). The results of this simulation suggest an optimal 3 dB coupling length of $17.0 \mu\text{m}$. The difference between the two values is due to extra coupling effects in the sine bends. From the MZI measurements discussed in Sec. II D, we can extract the performance of the couplers.

D. Mach-Zehnder interferometers (MMI and DC)

Tunable MZIs are a key component in QPICs, playing an important role for numerous functions, including as reconfigurable postselected entangling gates (R-PEGs),⁴⁹ demultiplexers,⁵⁰ variable beam splitters,⁵¹ filters,⁵² and single photon quantum logic gates.⁵³ In an MZI, a 3 dB coupler splits light evenly into two different paths that may be equal (balanced MZI) or unequal (unbalanced MZI) in length, which then recombine with another coupler. Here, we focus on two variations of thermo-optically tunable unbalanced MZIs employing both DCs and MMIs. These devices were designed

using the transfer matrix method,⁵⁴ where each component of the MZI can be represented by a matrix, two equivalent matrices for the 3 dB couplers, and a standalone matrix representing the path imbalance. Since many MZIs are required for a complete QPIC, the loss across each device must be minimized. Each coupler also should exhibit as close to a 3 dB splitting ratio as possible to achieve a maximum extinction ratio (ER), defined here as the power ratio of neighboring MZI fringes in the transmission spectrum.

Figure 6(a) shows an optical image of an MZI utilizing DCs as couplers with a $45 \mu\text{m}$ path imbalance on the top arm with the metal thermal tuner above the $1 \mu\text{m}$ thick cladding to sweep and control the MZI phase. One advantage of thermo-optic tuning with AlGaAs is its inherent large thermo-optic coefficient, which, for an MZI with a $60 \mu\text{m}$ path imbalance and a 10.28 nm free spectral range (FSR), allows for a full 2π phase sweep with $20 \text{ mW}/\pi$ efficiency, which is 10 (0.6) times more efficient than silicon nitride⁵⁵ (silicon⁵⁶). The transmission spectrum of MZIs with MMIs and DCs are shown in Figs. 6(b) and 6(c), respectively, for two different input/output configurations. We observe an ER above 10 dB across $\geq 100 \text{ nm}$ bandwidth for through ports and $\geq 200 \text{ nm}$ for cross ports, comparable to silicon MZIs.^{52,57} With the wavelength-dependent ER measurements, the true coupling coefficient κ of each coupler can be extracted,⁵⁴ as shown in Fig. 6(d). The DC (MMI) couplers exhibit an average coupling coefficient of 0.501 ± 0.03 (0.52 ± 0.11) across a 100 (200) nm bandwidth centered at 1570 (1550) nm, respectively.

III. QUBIT DE-MULTIPLEXING

To benchmark our platform, we perform a qubit de-multiplexing experiment in which entangled signal and idler photons generated from SFWM in a microring resonator are separated on-chip using a tunable unbalanced MZI with an

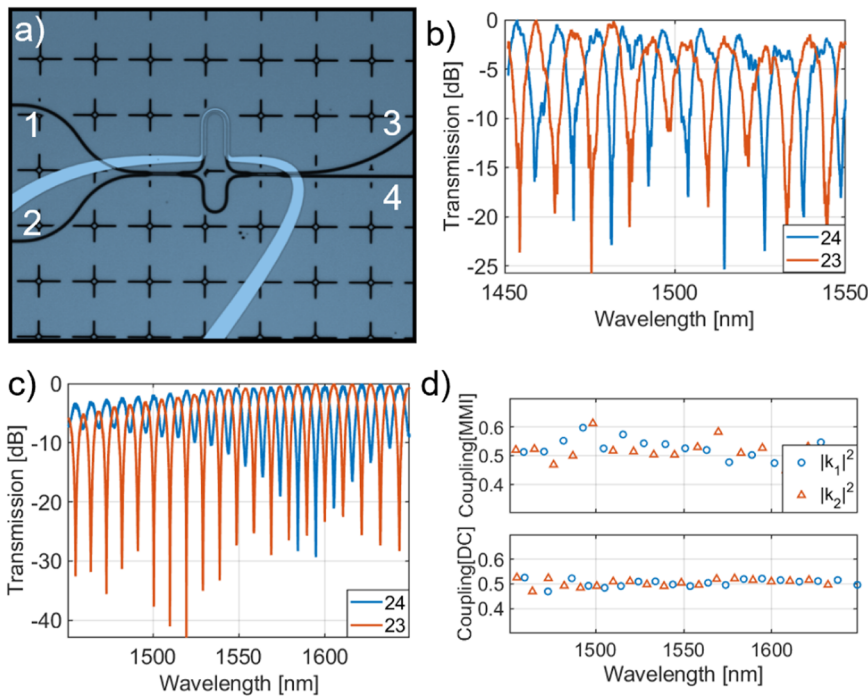


FIG. 6. (a) Optical image of an MZI with DCs and a 30 μm path imbalance. (b) and (c) Transmission spectra of the 2-4 and 2-3 port combinations of an MZI with MMIs (b) and DCs (c). (d) Extracted coupling coefficients for the DCs and MMIs in the MZIs indicating near-optimal 3-dB coupling.

FSR equal to twice the signal/idler mode separation. The experimental setup schematic is shown in Fig. 7(a). The chip temperature is stabilized with a thermo-electric cooler and control electronics. A tunable, narrow-linewidth continuous wave (cw) laser is tuned

into resonance with a microresonator mode near 1555 nm. Tunable etalon-based bandpass filters are tuned to the pump wavelength and placed immediately after the laser to suppress amplified spontaneous emission at the wavelengths of the signal and idler

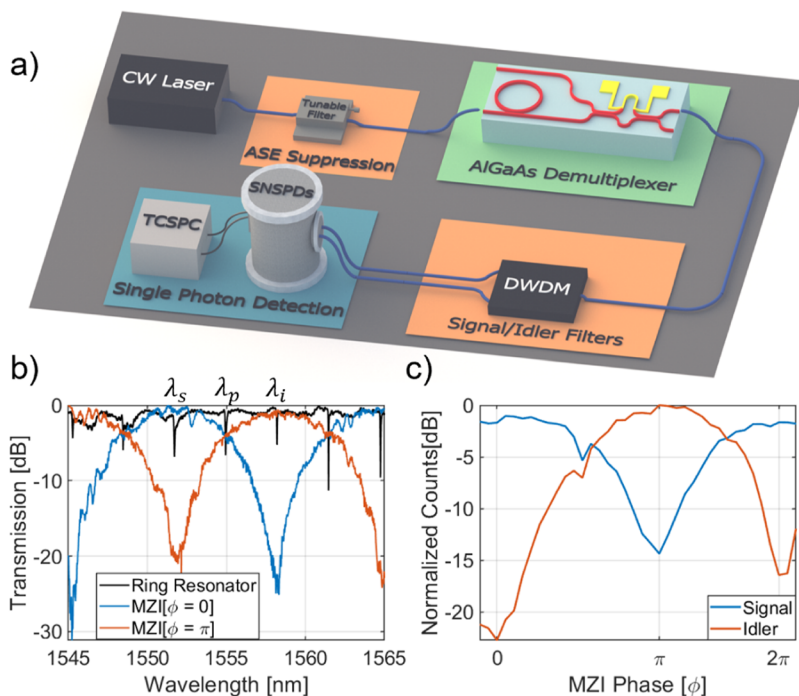


FIG. 7. (a) Experimental schematic of qubit de-multiplexing utilizing an 3.2 nm FSR AIGaAs ring resonator source and a 13.0 nm FSR MZI (DC). (b) Transmission spectra of a ring resonator and MZI tuned to a relative phase of zero and π radians. The signal, pump, and idler wavelengths are indicated. (c) Normalized counts on the SNSPDs after de-multiplexing as the MZI phase is swept from 0 to 2π radians.

modes, which helps ensure that pump photons do not reach the single-photon detectors in the experiment. The laser is polarized along the TE mode of the input waveguide, and light is coupled onto the chip with high-numerical aperture lensed fiber. Pump light is coupled into the microring resonator using a critically coupled pulley coupler, where the time-energy entangled signal and idler photon pairs are generated. The signal, idler, and pump photons are routed through the tunable MZI. When the phase of the MZI is properly tuned, it de-multiplexes the signal and idler photons into separate waveguides. Light from one output port is coupled off chip using a lensed polarization-maintaining single-mode fiber. The output is then sent to superconducting nanowire single-photon detectors (SNSPDs). Narrowband dense wavelength division multiplexing (DWDM) filters are placed in front of the SNSPDs to ensure that only detector 1 measures signal photons and detector 2 measures idler photons; these are in place for characterizing the chip, but their extinction ratio is >40 dB and thus they have no impact on the performance of the qubit de-multiplexing chip.

The chip is designed with an MZI with directional couplers and a $45.4 \mu\text{m}$ path imbalance for these experiments, which results in an MZI FSR that is equal to twice the signal/idler mode spacing of the microring resonator entangled-photon pair source. Figure 7(b) shows the transmission spectrum of the MZI chip when coupling into port 1 and out of port 4 for two different thermo-optic heater voltages corresponding to interferometer phase $\phi = 0$ and $\phi = \pi$ radians, respectively. The maximum MZI extinction is ~ 23 dB near the signal and idler wavelengths. As the phase is swept from 0 to π , the transmission at a single wavelength sweeps from maximum to minimum. Vertical lines in the plot depict the wavelengths of the pump (1555.0 nm), signal (1551.7 nm), and idler (1558.2 nm) photons from the microring resonator. We next pump the resonator to generate entangled pairs, which propagate through the MZI for de-multiplexing. Normalized counts from the two SNSPDs are shown in Fig. 7(c) as a function of the MZI phase. We measure an extinction ratio up to ~ 23 dB, which is identical to the measured MZI extinction ratio shown in Fig. 7(b) obtained from the transmission spectrum.

TABLE I. Table comparing the AlGaAsOI platform with SOI and Si_3N_4 designed for integrated quantum photonics.

	AlGaAsOI (this work)	SOI	Si_3N_4
Inverse taper			
Coupling loss	2.9 dB	<3 dB ³⁵	2–3 dB ⁶⁰
Waveguide crossing	0.23 dB	0.2 dB ⁴⁵	0.3 dB ⁴⁶
Loss			
MZI extinction Ratio	>30 dB	>30 dB ⁶¹	>40 dB ⁶²
MZI bandwidth (>10 dB ER)	200 nm cross 90 nm through	>40 nm ⁵⁷	180 nm ⁶²
MZI heater	20 mW/ π	12 mW/ π ⁵⁶	200 mW/ π ⁵⁵
Efficiency	(10.2 nm FSR)	(5.8 nm FSR)	(NA)

IV. CONCLUSION

Here we demonstrate many of the fundamental components necessary to develop fully integrated quantum photonic circuits on AlGaAsOI. With high-quality entangled photon pair sources²⁴ and the efficient edge couplers, 3 dB splitters, waveguide crossings, and MZIs demonstrated in this paper, a plethora of application-oriented integrated quantum circuits becomes available. Demonstrations of chip-to-chip quantum teleportation,³ multi-photon quantum information processing,⁵³ and other large-scale quantum photonic circuits have already been realized on the SOI platform.^{1,58} The benefits of the AlGaAsOI platform should enable more efficient demonstrations of these circuits at significantly lower optical pump power, reducing the required time to collect useful data and allowing for larger-scale circuits to be created. A summary of a few of the components discussed in this report is shown in Table I along with the performances of comparable components made on the SOI and Si_3N_4 platforms, which are also commonly used for quantum photonic circuits. It is important to note that the selected device performances were for Si and Si_3N_4 components that follow similar designs to the AlGaAsOI components that are relevant and routinely used for QPICs. For example, edge couplers with 0.35 dB of loss have been fabricated using silicon with silicon nitride, but these were achieved with multiple layers.⁵⁹ Here we compare similar component designs across the three platforms—using only a single photonic layer and standard photolithography to fabricate the devices. Overall, the AlGaAsOI components have similar or better performance than their SOI and Si_3N_4 counterparts, indicating that AlGaAsOI-based photonic circuits will exhibit little-to-no degradation in performance compared to the current state-of-the-art platforms. Although the components detailed in this work were fabricated using a $22 \times 24 \text{ mm}^2$ bonded AlGaAs chip, wafer-scale bonding with compound-semiconductor-on-insulator is possible,^{27,28} enabling larger circuits to be created in the near future.

ACKNOWLEDGMENTS

This work was supported by the NSF Quantum Foundry through Q-AMASE-i Program (Award No. DMR-1906325), AFOSR YIP (Award No. FA9550-20-1-0150), and NSF (Award No. CAREER-2045246). We also gratefully acknowledge support from the Cisco Research University Gift Program.

AUTHOR DECLARATIONS

Conflict of Interest

The authors have no conflicts to disclose.

Author Contributions

J. E. Castro: Data curation (equal); Formal analysis (equal); Investigation (equal); Methodology (equal); Writing – original draft (equal); Writing – review & editing (equal). **T. J. Steiner:** Data curation (equal); Formal analysis (equal); Investigation (equal); Methodology (equal); Writing – original draft (equal); Writing – review & editing (equal). **L. Thiel:** Data curation (supporting); Formal analysis (supporting); Investigation (supporting); Methodology

(supporting); Writing – original draft (supporting); Writing – review & editing (supporting). **A. Dinkelacker:** Investigation (supporting); Methodology (supporting); Writing – original draft (supporting); Writing – review & editing (supporting). **C. McDonald:** Investigation (supporting); Methodology (supporting); Writing – original draft (supporting); Writing – review & editing (supporting). **P. Pintus:** Data curation (supporting); Formal analysis (supporting); Investigation (supporting); Methodology (supporting); Writing – original draft (supporting); Writing – review & editing (supporting). **L. Chang:** Investigation (supporting); Methodology (supporting); Writing – original draft (supporting); Writing – review & editing (supporting). **J. E. Bowers:** Conceptualization (supporting); Funding acquisition (supporting); Project administration (supporting); Supervision (equal); Writing – original draft (supporting); Writing – review & editing (supporting). **G. Moody:** Conceptualization (lead); Data curation (supporting); Formal analysis (supporting); Funding acquisition (lead); Investigation (supporting); Methodology (supporting); Project administration (lead); Supervision (equal); Writing – original draft (supporting); Writing – review & editing (supporting).

DATA AVAILABILITY

The data that support the findings of this study are available from the corresponding author upon reasonable request.

REFERENCES

- G. Moody, L. Chang, T. J. Steiner, and J. E. Bowers, “Chip-scale nonlinear photonics for quantum light generation,” *AVS Quantum Sci.* **2**, 041702 (2020).
- C. Vigliar, S. Paesani, Y. Ding, J. C. Adcock, J. Wang, S. Morley-Short, D. Bacco, L. K. Oxenlowe, M. G. Thompson, J. G. Rarity, and A. Laing, “Error-protected qubits in a silicon photonic chip,” *Nat. Phys.* **17**, 1137–1143 (2021).
- D. Llewellyn, Y. Ding, I. I. Faruque, S. Paesani, D. Bacco, R. Santagati, Y.-J. Qian, Y. Li, Y.-F. Xiao, M. Huber, M. Malik, G. F. Sinclair, X. Zhou, K. Rottwitz, J. L. O’Brien, J. G. Rarity, Q. Gong, L. K. Oxenlowe, J. Wang, and M. G. Thompson, “Chip-to-chip quantum teleportation and multi-photon entanglement in silicon,” *Nat. Phys.* **16**, 148–153 (2019).
- J. M. Arrazola, V. Bergholm, K. Brádler, T. R. Bromley, M. J. Collins, I. Dhand, A. Fumagalli, T. Gerrits, A. Goussev, L. G. Helt, J. Hundal, T. Isacsson, R. B. Israel, J. Izaac, S. Jahangiri, R. Janik, N. Killoran, S. P. Kumar, J. Lavoie, A. E. Kita, D. H. Mahler, M. Menotti, B. Morrison, S. W. Nam, L. Neuhaus, H. Y. Qi, N. Quesada, A. Repeating, K. K. Sabapathy, M. Schuld, D. Su, J. Swinerton, A. Száva, K. Tan, P. Tan, V. D. Vaidya, Z. Vernon, Z. Zabaneh, and Y. Zhang, “Quantum circuits with many photons on a programmable nanophotonic chip,” *Nature* **591**, 54–60 (2021).
- Y. Zhao, Y. Okawachi, J. K. Jang, X. Ji, M. Lipson, and A. L. Gaeta, “Near-degenerate quadrature-squeezed vacuum generation on a silicon-nitride chip,” *Phys. Rev. Lett.* **124**, 193601 (2020); [arXiv:2002.001082](https://arxiv.org/abs/2002.001082).
- J. Wang, S. Paesani, Y. Ding, R. Santagati, P. Skrzypczyk, A. Salavrakos, J. Tura, R. Augusiak, L. Mancinska, D. Bacco, D. Bonneau, J. W. Silverstone, Q. Gong, A. Acín, K. Rottwitz, L. K. Oxenlowe, J. L. O’Brien, A. Laing, and M. G. Thompson, “Multidimensional quantum entanglement with large-scale integrated optics,” *Science* **360**, 285–291 (2018); [arXiv:1803.04449](https://arxiv.org/abs/1803.04449).
- G. Moody, V. J. Sorger, D. J. Blumenthal, P. W. Juodawlkis, W. Loh, C. Sorace-Agaskar, A. E. Jones, K. C. Balram, J. C. F. Matthews, A. Laing *et al.*, “2022 Roadmap on integrated quantum photonics,” *J. Phys.: Photonics* **4**, 012501 (2022).
- C. Ma, X. Wang, V. Anant, A. D. Beyer, M. D. Shaw, and S. Mookherjee, “Silicon photonic entangled photon-pair and heralded single photon generation with CAR >12,000 and $g_0^{(2)} < 0.006$,” *Opt. Express* **25**, 32995–33006 (2017).
- J. A. Jaramillo-Villegas, P. Imany, O. D. Odele, D. E. Leaird, Z.-Y. Ou, M. Qi, and A. M. Weiner, “Persistent energy-time entanglement covering multiple resonances of an on-chip biphoton frequency comb,” *Optica* **4**(6), 655–658 (2017).
- X. Guo, C.-I. Zou, C. Schuck, H. Jung, R. Cheng, and H. X. Tang, “Parametric down-conversion photon-pair source on a nanophotonic chip,” *Light: Sci. Appl.* **6**, e16249 (2016).
- J. Zhao, C. Ma, M. Rüsing, and S. Mookherjee, “High quality entangled photon pair generation in periodically poled thin-film lithium niobate waveguides,” *Phys. Rev. Lett.* **124**, 163603 (2020).
- A. Boes, B. Corcoran, L. Chang, J. Bowers, and A. Mitchell, “Status and potential of lithium niobate on insulator (LNOI) for photonic integrated circuits,” *Laser Photonics Rev.* **12**, 1700256 (2018).
- R. R. Kumar, M. Raevskaia, V. Pogoretskii, Y. Jiao, and H. K. Tsang, “Entangled photon pair generation from an InP membrane micro-ring resonator,” *Appl. Phys. Lett.* **114**, 021104 (2019).
- W. Xie, L. Chang, H. Shu, J. C. Norman, J. D. Peters, X. Wang, and J. E. Bowers, “Ultra-high-Q AlGaAs-on-insulator microresonators for integrated nonlinear photonics,” *Opt. Express* **28**, 32894–32906 (2020).
- L. Ottaviano, M. Pu, E. Semenova, and K. Yvind, “Low-loss high-confinement waveguides and microring resonators in AlGaAs-on-insulator,” *Opt. Lett.* **41**, 3996–3999 (2016).
- J. Komma, C. Schwarz, G. Hofmann, D. Heinert, and R. Nawrodt, “Thermo-optic coefficient of silicon at 1550 nm and cryogenic temperatures,” *Appl. Phys. Lett.* **101**, 041905 (2012).
- G. Cocorullo, F. G. Della Corte, and I. Rendina, “Temperature dependence of the thermo-optic coefficient in crystalline silicon between room temperature and 550 K at the wavelength of 1523 nm,” *Appl. Phys. Lett.* **74**, 3338 (1999).
- F. G. Della Corte, G. Cocorullo, M. Iodice, and I. Rendina, “Temperature dependence of the thermo-optic coefficient of InP, GaAs, and SiC from room temperature to 600 K at the wavelength of 1.5 μm ,” *Appl. Phys. Lett.* **77**, 1614 (2000).
- R. Walker, N. Cameron, Y. Zhou, C. Main, G. Hoy, and S. Clements, “50GHz gallium arsenide electro-optic modulators for spaceborne telecommunications,” *Proc. SPIE* **11180**, 111807G (2019).
- M. Forsch, R. Stockill, A. Wallucks, I. Marinković, C. Gärtner, R. A. Norte, F. van Otten, A. Fiore, K. Srinivasan, and S. Gröblacher, “Microwave-to-optics conversion using a mechanical oscillator in its quantum ground state,” *Nat. Phys.* **16**, 69–74 (2020).
- S. Adachi, *GaAs and Related Materials* (World Scientific, 1994).
- S. Mariani, A. Andronico, A. Lemaître, I. Faverio, S. Ducci, and G. Leo, “Second-harmonic generation in AlGaAs microdisks in the telecom range,” *Opt. Lett.* **39**, 3062–3065 (2014).
- L. Chang, W. Xie, H. Shu, Q. F. Yang, B. Shen, A. Boes, J. D. Peters, W. Jin, C. Xiang, S. Liu, G. Moille, S. P. Yu, X. Wang, K. Srinivasan, S. B. Papp, K. Vahala, and J. E. Bowers, “Ultra-efficient frequency comb generation in AlGaAs-on-insulator microresonators,” *Nat. Commun.* **11**, 1331 (2020).
- T. J. Steiner, J. E. Castro, L. Chang, Q. Dang, W. Xie, J. Norman, J. E. Bowers, and G. Moody, “Ultrabright entangled-photon-pair generation from an AlGaAs-on-insulator microring resonator,” *PRX Quantum* **2**, 010337 (2021).
- E. Knill, R. Laflamme, and G. J. Milburn, “A scheme for efficient quantum computation with linear optics,” *Nature* **409**, 46–52 (2001).
- C. McDonald, G. Moody, S. W. Nam, R. P. Mirin, J. M. Shainline, A. McCaughan, S. Buckley, and K. L. Silverman, “III-V photonic integrated circuit with waveguide-coupled light-emitting diodes and WSi superconducting single-photon detectors,” *Appl. Phys. Lett.* **115**, 081105 (2019).
- E. J. Stanton, J. Chiles, N. Nader, G. Moody, N. Volet, L. Chang, J. E. Bowers, S. Woo Nam, and R. P. Mirin, “Efficient second harmonic generation in nanophotonic GaAs-on-insulator waveguides,” *Opt. Express* **28**, 9521 (2020); [arXiv:1912.12346](https://arxiv.org/abs/1912.12346).
- L. Chang, G. D. Cole, G. Moody, and J. E. Bowers, “CSOI: Beyond silicon-on-insulator photonics,” *Opt. Photonics News* **33**, 24–31 (2022).
- A. L. Gaeta, M. Lipson, and T. J. Kippenberg, “Photonic-chip-based frequency combs,” *Nat. Photonics* **13**(3), 158–169 (2019).
- T. J. Kippenberg, A. L. Gaeta, M. Lipson, and M. L. Gorodetsky, “Dissipative Kerr solitons in optical microresonators,” *Science* **361**, eaan8083 (2018).

- ³¹D. T. Spencer, T. Drake, T. C. Briles, J. Stone, L. C. Sinclair, C. Fredrick, Q. Li, D. Westly, B. R. Ilic, A. Bluestone, N. Volet, T. Komljenovic, L. Chang, S. H. Lee, D. Y. Oh, M. G. Suh, K. Y. Yang, M. H. P. Pfeiffer, T. J. Kippenberg, E. Norberg, L. Theogarajan, K. Vahala, N. R. Newbury, K. Srinivasan, J. E. Bowers, S. A. Diddams, and S. B. Papp, "An optical-frequency synthesizer using integrated photonics," *Nature* **557**(7703), 81–85 (2018).
- ³²R. Marchetti, C. Lacava, L. Carroll, K. Gradkowski, and P. Minzioni, "Coupling strategies for silicon photonics integrated chips [Invited]," *Photonics Res.* **7**, 201 (2019).
- ³³L. Cheng, S. Mao, Z. Li, Y. Han, and H. Y. Fu, "Grating couplers on silicon photonics: Design principles, emerging trends and practical issues," *Micromachines* **11**, 666 (2020).
- ³⁴D. Taillaert, F. Van Laere, M. Ayre, W. Bogaerts, D. Van Thourhout, P. Bienstman, and R. Baets, "Grating couplers for coupling between optical fibers and nanophotonic waveguides," *Jpn. J. Appl. Phys.* **45**, 6071–6077 (2006).
- ³⁵X. Mu, S. Wu, L. Cheng, and H. Y. Fu, "Edge couplers in silicon photonic integrated circuits: A review," *Appl. Sci.* **10**, 1538 (2020).
- ³⁶Y. Liu and J. Yu, "Low-loss coupler between fiber and waveguide based on silicon-on-insulator slot waveguides," *Appl. Opt.* **46**, 7858–7861 (2007).
- ³⁷G. Roelkens, P. Dumon, W. Bogaerts, D. Van Thourhout, and R. Baets, "Efficient silicon-on-insulator fiber coupler fabricated using 248-nm-deep UV lithography," *IEEE Photonics Technol. Lett.* **17**, 2613–2615 (2005).
- ³⁸Q. Fang, T.-Y. Liow, J. F. Song, C. W. Tan, M. B. Yu, G. Q. Lo, and D.-L. Kwong, "Suspended optical fiber-to-waveguide mode size converter for silicon photonics," *Opt. Express* **18**, 7763 (2010).
- ³⁹A. V. Tsarev, "Efficient silicon wire waveguide crossing with negligible loss and crosstalk," *Opt. Express* **19**, 13732 (2011).
- ⁴⁰J. Chiles, S. Buckley, N. Nader, S. W. Nam, R. P. Mirin, and J. M. Shainline, "Multi-planar amorphous silicon photonics with compact interplanar couplers, cross talk mitigation, and low crossing loss," *APL Photonics* **2**, 116101 (2017).
- ⁴¹W. Chang and M. Zhang, "Silicon-based multimode waveguide crossings," *J. Phys.: Photonics* **2**, 022002 (2020).
- ⁴²W. Bogaerts, P. Dumon, D. V. Thourhout, and R. Baets, "Low-loss, low-crosstalk crossings for silicon-on-insulator nanophotonic waveguides," *Opt. Lett.* **32**, 2801 (2007).
- ⁴³S. Wu, X. Mu, L. Cheng, S. Mao, and H. Y. Fu, "State-of-the-art and perspectives on silicon waveguide crossings: A review," *Micromachines* **11**, 326 (2020).
- ⁴⁴P. J. Bock, P. Cheben, J. H. Schmid, J. Lapointe, A. Del age, D.-X. Xu, S. Janz, A. Densmore, and T. J. Hall, "Subwavelength grating crossings for silicon wire waveguides," *Opt. Express* **18**, 16146 (2010).
- ⁴⁵P. Sanchis, P. Villalba, F. Cuesta, A. H akansson, A. Griol, J. V. Gal an, A. Brimont, and J. Mart ı, "Highly efficient crossing structure for silicon-on-insulator waveguides," *Opt. Lett.* **34**, 2760 (2009).
- ⁴⁶H. Yang, P. Zheng, G. Hu, R. Zhang, B. Yun, and Y. Cui, "A broadband, low-crosstalk and low polarization dependent silicon nitride waveguide crossing based on the multimode-interference," *Opt. Commun.* **450**, 28–33 (2019).
- ⁴⁷T. Fukazawa, T. Hirano, F. Ohno, and T. Baba, "Low loss intersection of Si photonic wire waveguides," *Jpn. J. Appl. Phys.* **43**, 646–647 (2004).
- ⁴⁸Y. Zhang, A. Hosseini, X. Xu, D. Kwong, and R. T. Chen, "Ultralow-loss silicon waveguide crossing using Bloch modes in index-engineered cascaded multimode-interference couplers," *Opt. Lett.* **38**, 3608 (2013).
- ⁴⁹J. C. Adcock, S. Morley-Short, J. W. Silverstone, and M. G. Thompson, "Hard limits on the postselectability of optical graph states," *Quantum Sci. Technol.* **4**, 015010 (2018).
- ⁵⁰F. Horst, W. M. J. Green, S. Assefa, S. M. Shank, Y. A. Vlasov, and B. J. Offrein, "Cascaded Mach-Zehnder wavelength filters in silicon photonics for low loss and flat pass-band WDM (de-)multiplexing," *Opt. Express* **21**, 11652–11658 (2013).
- ⁵¹C. M. Wilkes, X. Qiang, J. Wang, R. Santagati, S. Paesani, X. Zhou, D. A. B. Miller, G. D. Marshall, M. G. Thompson, and J. L. O'Brien, "60 dB high-extinction auto-configured Mach-Zehnder interferometer," *Opt. Lett.* **41**, 5318–5321 (2016).
- ⁵²M. Piekarek, D. Bonneau, S. Miki, T. Yamashita, M. Fujiwara, M. Sasaki, H. Terai, M. G. Tanner, C. M. Natarajan, R. H. Hadfield, J. L. O'Brien, and M. G. Thompson, "Passive high-extinction integrated photonic filters for silicon quantum photonics," in *Conference on Lasers and Electro-Optics* (Optica Publishing Group, 2016), paper FM1N.6.
- ⁵³J. C. Adcock, C. Vigliar, R. Santagati, J. W. Silverstone, and M. G. Thompson, "Programmable four-photon graph states on a silicon chip," *Nat. Commun.* **10**(1), 3528 (2019).
- ⁵⁴M. A. Tran, T. Komljenovic, J. C. Hulme, M. L. Davenport, and J. E. Bowers, "A robust method for characterization of optical waveguides and couplers," *IEEE Photonics Technol. Lett.* **28**, 1517–1520 (2016).
- ⁵⁵J.-M. Lee, W.-J. Lee, M.-S. Kim, S. Cho, J. J. Ju, G. Navickaite, and J. Fernandez, "Controlled-NOT operation of SiN-photonic circuit using photon pairs from silicon-photonic circuit," *Opt. Commun.* **509**, 127863 (2022).
- ⁵⁶J.-M. Lee, M.-S. Kim, J. T. Ahn, L. Adelmini, D. Fowler, C. Kopp, C. J. Oton, and F. Testa, "Demonstration and fabrication tolerance study of temperature-insensitive silicon-photonic MZI tunable by a metal heater," *J. Lightwave Technol.* **35**, 4903–4909 (2017).
- ⁵⁷J.-M. Lee, W.-J. Lee, M.-S. Kim, and J. J. Ju, "Noise filtering for highly correlated photon pairs from silicon waveguides," *J. Lightwave Technol.* **37**, 5428–5434 (2019).
- ⁵⁸L. Lu, X. Zheng, Y. Lu, S. Zhu, and X. S. Ma, "Advances in chip-scale quantum photonic technologies," *Adv. Quantum Technol.* **4**, 2100068 (2021).
- ⁵⁹X. Wang, X. Quan, M. Liu, and X. Cheng, "Silicon-nitride-assisted edge coupler interfacing with high numerical aperture fiber," *IEEE Photonics Technol. Lett.* **31**, 349–352 (2019).
- ⁶⁰S. Ramelow, A. Farsi, S. Clemmen, D. Orquiza, K. Luke, M. Lipson, and A. L. Gaeta, "Silicon-nitride platform for narrowband entangled photon generation," *arXiv:1508.04358* (2015).
- ⁶¹J. Wang, D. Bonneau, M. Villa, J. W. Silverstone, R. Santagati, S. Miki, T. Yamashita, M. Fujiwara, M. Sasaki, H. Terai, M. G. Tanner, C. M. Natarajan, R. H. Hadfield, J. L. O'Brien, and M. G. Thompson, "Chip-to-chip quantum photonic interconnect by path-polarization interconversion," *Optica* **3**, 407–413 (2016).
- ⁶²A. Rao, G. Moille, X. Lu, D. Westly, M. Geiselman, M. Zervas, and K. Srinivasan, "Up to 50 dB extinction in broadband single-stage thermo-optic Mach-Zehnder interferometers for programmable low-loss silicon nitride photonic circuits," in *2021 Conference on Lasers and Electro-Optics* (Optica Publishing Group, 2021), paper SM1A.7.